PASJ: Publ. Astron. Soc. Japan **47**, 527–549 (1995)

Galactic-Center Molecular Arms, Ring, and Expanding Shell. I. Kinematical Structures in Longitude–Velocity Diagrams

Yoshiaki SOFUE
Institute of Astronomy, The University of Tokyo, Mitaka, Tokyo 181
sofue@mtk.ioa.s.u-tokyo.ac.jp

(Received 1994 September 19; accepted 1995 August 14)

Abstract

Analyzing the $(l, b, V_{\rm LSR})$ data cube of ^{13}CO($J = 1$–0)-line emission from the Bell-Telephone-Laboratory survey, we have investigated the molecular gas distribution and kinematics in the central $\pm 1°$ (± 150 pc) region of the Galaxy. We have applied the pressing method to remove the local- and foreground-gas components at low velocities in order to estimate the intensity more quantitatively. Two major dense molecular arms have been identified in longitude–radial velocity (l, V) diagrams as apparently rigidly-rotating ridges. The ridges are spatially identified as two arms, which we call the Galactic-Center molecular Arms (GCA). The arms compose a rotating ring of radius 120 pc (the 120-pc Molecular Ring), whose inclination is $i \simeq 85°$. The Sgr B molecular complex is associated with GCA I, and Sgr C complex is located on GCA II. These arms are as thin as 13 to 15 pc, except for vertically extended massive complexes around Sgr B and C. The (l, V) behavior of the arms can be qualitatively reproduced by a model which assumes spiral arms of gas. Assuming a small pitch angle for the arms, we tried to deconvolve the (l, V) diagram to a projection on the galactic plane, and present a possible face-on CO map as seen from the galactic pole, which also reveals a molecular ring and arms. We have estimated the masses of these molecular features, using the most recent value of the CO-to-H_2 conversion factor, taking into account its metallicity dependence and radial gradient in the Galaxy. The estimated molecular masses and kinetic energy are about a factor of three smaller than those reported in the literature using the conventional conversion factor.

Key words: Galaxy: center — Galaxy: kinematics and dynamics — Galaxy: structure — ISM: clouds — ISM: molecules

1. Introduction

The galactic center region has been extensively observed in the molecular lines, particularly in the CO line emission (Oort 1977; Scoville et al. 1974; Liszt 1988; Liszt, Burton 1978, 1980; Burton, Liszt 1983, 1992; Brown, Liszt 1984; Heiligman 1987; Bally et al. 1987, 1988; Genzel, Townes 1987; Stark et al. 1989; Güsten 1989). Besides the 4-kpc molecular ring, the CO emission is strongly concentrated in the central few degrees (Dame et al. 1987). Moreover, the molecular gas in the central region has a strong concentration within $|l| < 1°$ (150 pc) where the majority of the nuclear disk gas is confined (Scoville et al. 1974; Bally et al. 1987; Heiligman 1987). This high concentration of dense interstellar matter in a small region is also clearly visible in the far-IR emission (e.g., Cox, Laureijs 1989) and in the C II emission (Okuda et al. 1989). The radio continuum emission also indicates a highly concentrated nuclear disk of ionized gas (Altenhoff et al. 1978; Handa et al. 1987). On the other hand, the region between galactocentric distances ~ 200 pc ($l \sim 1°.4$) and ~ 2 kpc ($15°$) appears to be almost empty in the CO emission (Bally et al. 1987; Knapp et al. 1985).

The total molecular mass in the $|l| < 1°$ region, estimated from the CO emission amounts to $\sim 1.4 \times 10^8 M_\odot$ for a traditional CO-to-H_2 conversion factor, or, more probably, $\sim 4.6 \times 10^7 M_\odot$ for a new conversion factor (see section 3). On the other hand, the H I mass within the 1.2 kpc tilted disk ($l < 8°$) is only of several $10^6 M_\odot$ (Liszt, Burton 1980). Hence, we may consider that the central $\sim$1-kpc region is dominated by a molecular disk of ~ 150 pc ($\sim 1°$) radius, outside of which the gas density becomes an order of magnitude smaller.

Various molecular gas features in the central $\sim$ 100–200 pc region have been discussed by various authors, such as a disk related to the 1.2-kpc tilted rotating disk (Liszt, Burton 1980; Burton, Liszt 1992), molecular rings and spiral arms of a few hundred persec scale (Scoville et al. 1974; Heiligman 1987; Bally et al. 1987), small shell structures (Tsuboi 1989), and an expanding molecular ring of 200 pc radius (Scoville 1972; Kaifu et al. 1972,

1974). On the other hand, Binney et al. (1991) have modeled the "expanding-ring feature" or the "parallelogram" on the (l, V) (longitude–velocity) plot in terms of non-circular kinematics of gas by a closed-orbit model in a bar potential. It is known that the gas in this parallelogram shares only a small fraction of the total molecular mass in the galactic center: the majority of the gas composes more rigid-body like features in the (l, V) plots.

The CO gas in the central few hundred parsecs regions in nearby galaxies has been observed by high-resolution mm-wave interferometry, and the distribution and kinematics have been extensively studied (e.g., Lo et al. 1984; Ishiguro et al. 1989; Ishizuki et al. 1990a, b). The central gas disks of galaxies appear to comprise spiral arms or circum-nuclear rings of a few hundred pc size. Such a gaseous behavior can be reproduced to some extent by theoretical simulations of the accretion of gas clouds in a central gravitational potential (e.g., Noguchi 1988; Wada, Habe 1992).

In this paper, we revisit the major part of the nuclear molecular disk ($|l| \lesssim 1°$) by analyzing the molecular line data under the premise that the nuclear disk may comprise accretion ring or spiral structures similar to those found in external galaxies. In this paper we reanalyze the data cube of the ^{13}CO (J = 1–0)-line emission observed by Bally et al. (1987) with the 7-m off-set Cassegrain telescope of the Bell Telephone Laboratory. The distance to the Galactic Center is assumed to be 8.5 kpc throughout this paper.

2. Longitude-Velocity (l, V) Diagrams

2.1. Data

The angular resolution of the observations with the Bell-Telephone 7-m antenna at the ^{13}CO line was 1.′7. The data used here are in a $(l, b, V_{\rm LSR})$ cube in the FITS format. The cube covers an area of $-1.°1 \leq l \leq 0.°92$, $-21' \leq b \leq 17'$, or 300 pc × 94 pc for a 8.5 kpc distance. The velocity coverage is $-250 \leq V_{\rm LSR} \leq 250$ km s^{-1}. The cube comprises 127, 39, and 183 channels at 1′, 1′, and 2.75 km s^{-1} intervals, respectively. We also use the CS line data in a (l, b, V) cube with dimensions of 151, 42, and 163 channels at intervals 2′, 1′, and 2.75 km s^{-1}, which covers an area of $-1° \leq l \leq 4°$, $-25' \leq b \leq 16'$, and $-250 \leq V_{\rm LSR} \leq 190$ km s^{-1}. The intensity scale of the data is the main-beam antenna temperature, which is approximately equivalent to the brightness temperature in Kelvin. The observational details have been described in Bally et al. (1987, 1988). We made use of the AIPS and IRAF software packages for the reduction.

2.2. Subtraction of the Local and Foreground Components

In order to analyze the molecular gas features in the Galactic-Center region, we first subtract contamination by local and foreground molecular clouds at low velocities. Since the ^{13}CO line is optically thin for the foreground clouds, the contamination appears as emission stripes superposed on the galactic-center emission. The subtraction of foreground emission is essential when we derive the mass and kinetic energy of the molecular gas features. Such a "cleaning" also helps in the morphological recognition of features on the (l, V) and (b, V) diagrams.

Figure 1a shows an (l, V) diagram averaged at a latitude range of $-17' \leq b \leq 12'$. The diagram is strongly affected by "stripes" at low velocities elongated in the direction of longitude with narrow velocity widths, including the 3-kpc expanding arm at -52 km s^{-1}. In order to eliminate these stripes, we applied the "pressing method", which was developed for removing scanning effects in raster scan observations (Sofue, Reich 1979). We briefly describe this method below.

The original (l, V) map M_0 is trimmed by $-70 \leq V_{\rm LSR} \leq 50$ km s^{-1} to yield M_1, where the local and foreground gas contributions are significant. The trimmed map M_1 is smoothed only in the V direction by 5 channels (14 km s^{-1}) using a boxcar or Gaussian smoothing task of IRAF yielding M_2. The smoothed map M_2 is subtracted from M_1 to yield M_3 ($= M_1 - M_2$). Map M_3 is then smoothed only in the l direction by 20 channels (20′) (boxcar or Gaussian) to yield M_4. This M_4 map approximates the contribution from the local gas that is dominated by elongated features in the longitudinal direction. We then subtract M_4 from M_1 to obtain M_5 ($= M_1 - M_4$). This M_5 is, thus, a map in which the local gas contribution has been roughly subtracted. M_5 is then smoothed in the V direction by 5 channels. We then replace M_2 by this smoothed map, and repeat the above procedures twice (or more times) until we obtain the second (or n-th) M_5. Finally, the $-70 \leq V_{\rm LSR} \leq 50$ km s^{-1} part of the original map M_0 is replaced by M_5 to yield M_6. Now, we have a "pressed" map M_6 in which corrugations due to local gas clouds have been removed. Figure 1b shows the thus obtained map M_6 for the same (l, V) diagram as in figure 1a.

We applied this algorithm (the pressing method) to all (l, V) and (b, V) diagrams in the cube, and created a new (l, b, V) cube, which is almost free from local and foreground contaminations. In the present paper we use this new cube. We also applied the pressing method to remove scanning effects, which had originated during the data acquisition, in every diagram, such as intensity maps in the (l, b) space.

By comparing the original and the thus-'pressed' maps, we estimated the contribution of the local/foreground

emission to be 5% of the total emission, and 9% of the emission with $|V_{\rm LSR}| < 100$ km s^{-1}. Therefore, without subtraction, the mass and energetics would be overestimated by about 5 to 9%. Moreover, if the gas out of the disk component at $|b| > 10'$ is concerned, this local contribution would amount to more than 10%. Hence, subtraction of the foreground emissions is crucial in a quantitative consideration of the features discussed in this paper.

2.3. *"Arms" in Longitude-Velocity (l, V) Diagrams*

Figure 2 shows (l, V) diagrams near to the galactic plane averaged over a 4′ latitude interval after subtraction of the local/foreground components. Various features found in these diagrams have been discussed by Bally et al. (1987, 1988). In this paper we highlight continuous features (ridges) traced in the (l, V) diagrams. The major structures of the "disk component" at low latitude ($|b| \lesssim 10'$=25 pc) are "rigid-rotation" ridges, which we call "arms". Figure 3 illustrates these ridges (arms), which can be identified in the diagrams as coherent structures. In table 1 we summarize the identified features, and describe below the individual arms. Heiligman (1987) has used these ridges to derive a rigid-rotation curve. At higher latitudes ($|b| \gtrsim 10'$) the so-called expanding ring features appear at high velocities ($|V_{\rm LSR}| > 100$ km s^{-1}), which will be discussed in a separate paper.

2.3.1. *Arm I*

The most prominent (l, V) arm is found as a long and straight ridge, slightly above the galactic plane at $b \sim 2'$, which runs from (l, V)=(0.°9, 80 km s^{-1}) to (−0.°7, −150 km s^{-1}), and extends to (−1.°0, −200 km s^{-1}). This arm intersects the line at $l = 0°$ at negative velocity, $V_{\rm LSR} = -40$ km s^{-1}, indicating that the gas is approaching us at $l = 0°$. We call this ridge Arm I. A part of this arm can also be traced below the galactic plane at $b = -0.°1$, running from (l, V)=(0.°8, 60 km s^{-1}) to (0.°1, −20 km s^{-1}). Its positive longitude part is connected to the dense molecular complex Sgr B, which is extended both in space and velocity, from $b = -0.25$ to 0.°07 and $V_{\rm LSR}$=20 to 100 km s^{-1}.

2.3.2. *Arm II*

Another prominent arm is seen at negative latitude at $b \sim -6'$, running from (l, V)=(0.°1, 60 km s^{-1}) to (−0.°6, −80 km s^{-1}). We call this ridge Arm II. It is bent at $l \sim 0.°1$ and appears to continue to (l, V)=(1°, 100 km s^{-1}), and merges with Arm I at the Sgr B complex region. The negative longitude part also merges with Arm I, and is connected to the Sgr C complex. Arm II intersects $l = 0°$ at a positive velocity of $V_{\rm LSR} = 50$ km s^{-1}.

2.3.3. *Arms III and IV*

At positive latitude ($b \sim 0.°01$ to 0.°2), another arm can be traced running from (l, V)=(0°, 140 km s^{-1}) to (−0.°15, 10 km s^{-1}). Its counterpart to the negative longitude side appears to be present at (l, V)=(−0.°45, −120 km s^{-1}) to (−0.°55, −180 km s^{-1}). We call this ridge Arm III. Bally et al. (1988) called this the "polar arc", and discussed its connection to Sgr A.

A branch can be traced from (l, V)=(0.°1, 60 km s^{-1}) to (0°, −20 km s^{-1}), apparently being bifurcated from Arm II at $l \sim 0.°1$. This ridge intersects $l = 0°$ at negative velocity ($V_{\rm LSR} = -50$ km s^{-1}). We call this ridge Arm IV.

2.4. *"Rigid-rotation" in (l, V) Plane and "Arms and Ring" in the Galactic Plane*

We emphasize that "rigid-rotation" ridges in (l, V) diagrams for edge-on galaxies, whose rotation curves are usually flat, are generally interpreted as being due to spiral arms and rings. Indeed, the rigid-rotation ridge in the CO (l, V) diagram of the Milky Way is identified by the 4-kpc molecular ring (e.g., Dame et al. 1987; Combes 1992). Many edge-on spiral galaxies like NGC 891 are found to show similar (l, V) ridges in H I and CO, which are also interpreted as being spiral arms and rings (e.g., Sofue, Nakai 1993, 1994).

The circular rotation velocity, defined by $V_{\rm rot} = (R\partial\Phi/\partial R)^{1/2}$, remains greater than at least 150 km s^{-1} from the nuclear few pc region until the 1 kpc radius region (Genzel, Townes 1987). Here, Φ is the potential and R is the distance from the nucleus. Hence, the actual rotation should not be rigid at all. The rigid-rotation ridges in the (l, V) plane such as Arms I to IV in the Galactic Center can thus be more naturally attributed to real arms and rings.

3. Intensity Distribution and the Galactic Center Arms

3.1. *Intensity Maps and Masses*

Figure 4a shows the total intensity map integrated over the full range of the velocity ($-250 \le V_{\rm LSR} \le 250$ km s^{-1}). This map is about the same as that presented by Stark et al. (1989), except that the local gas has been removed. Figure 4b shows the same in gray scale and that with the vertical scale in the b direction enlarged twice.

First of all, the intensity map can be used to obtain the molecular mass. However, the conversion of the CO intensity to H_2 mass is not straightforward. We have recently studied the correlation of the conversion factor X_{12} for the ^{12}CO(J = 1–0) line the metal abundance in galaxies (Arimoto et al. 1994). We have obtained a clear dependence of X on the galacto-centric distance R

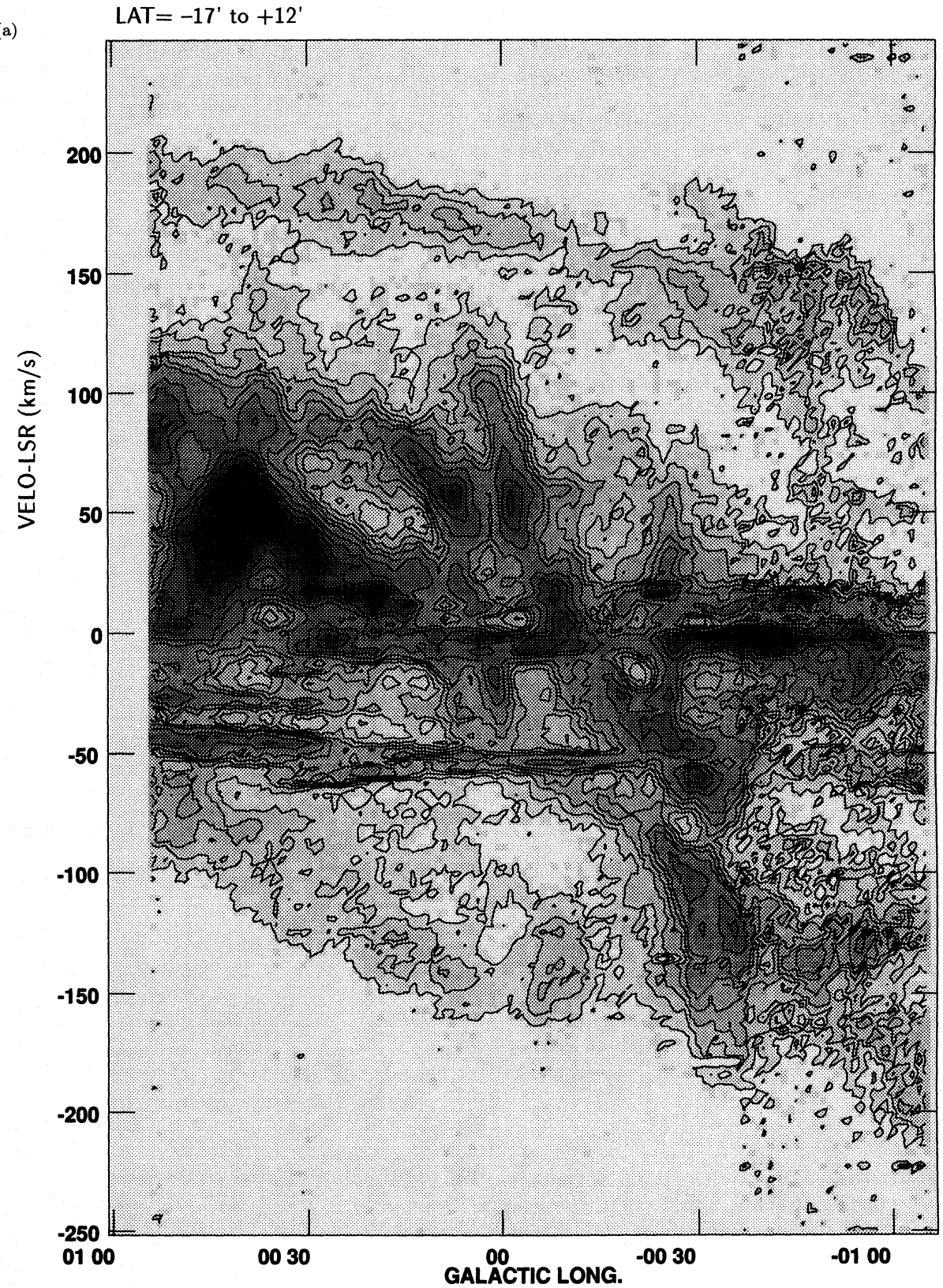

Fig. 1. (a) The (l, V) diagram of the ^{13}CO ($J = 1$–0) line emission of the central region of the Milky Way by averaging the data from $-0.^{\circ}35 \leq b \leq 0.^{\circ}17$ as obtained with the Bell Telephone 7-m telescope by Bally et al. (1987). The contours are in units of K $T_{\rm A}^{*}$ at levels $0.1\times(1, 2, 3, 4, 5, 6, 8, 12, 15, 20, 25)$.

(b)

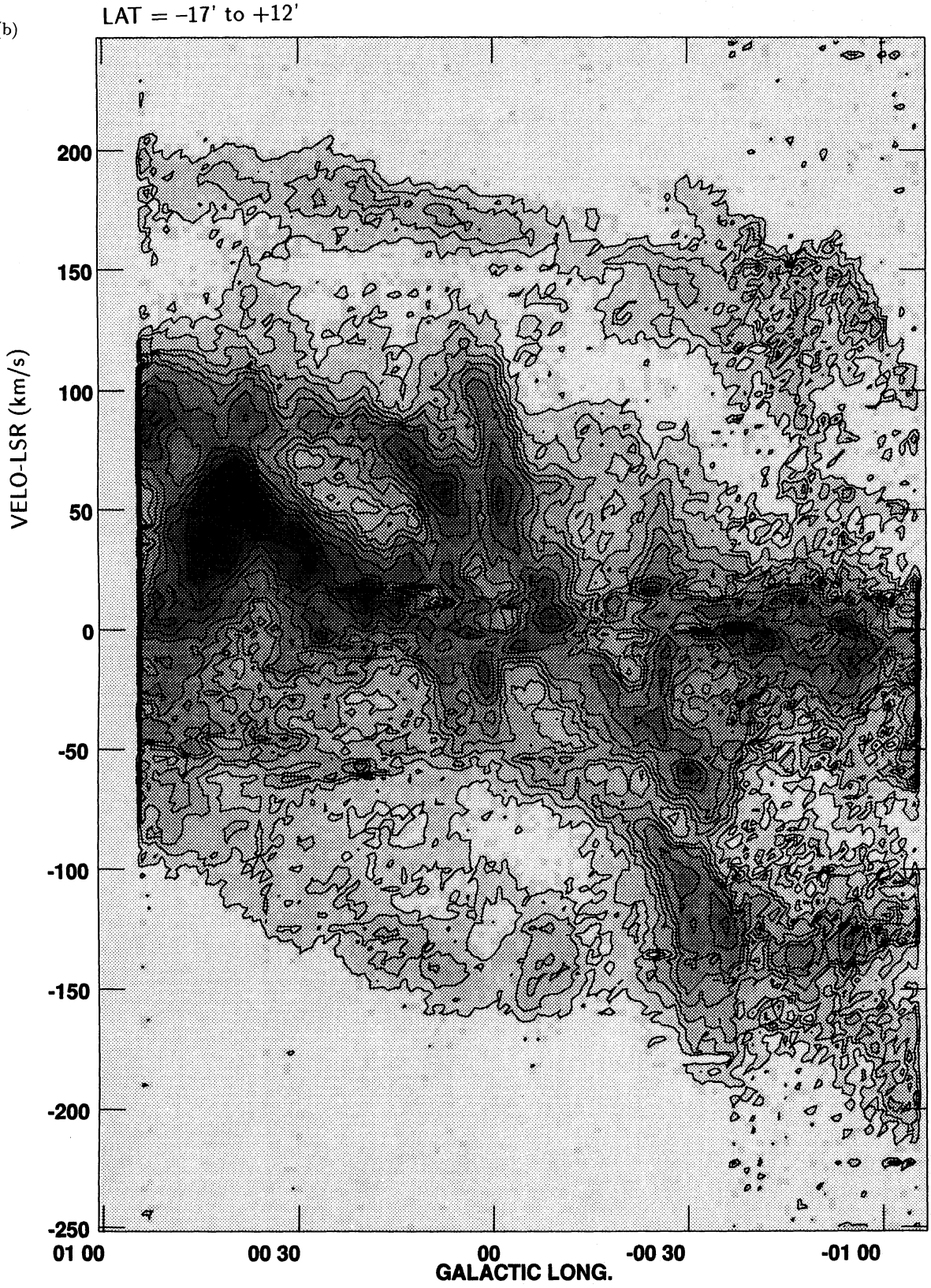

Fig. 1. (b) Same as (a), but the local and foreground CO emissions have been subtracted by applying the "pressing method" (see the text for the procedure). The contour levels are the same as in (a).

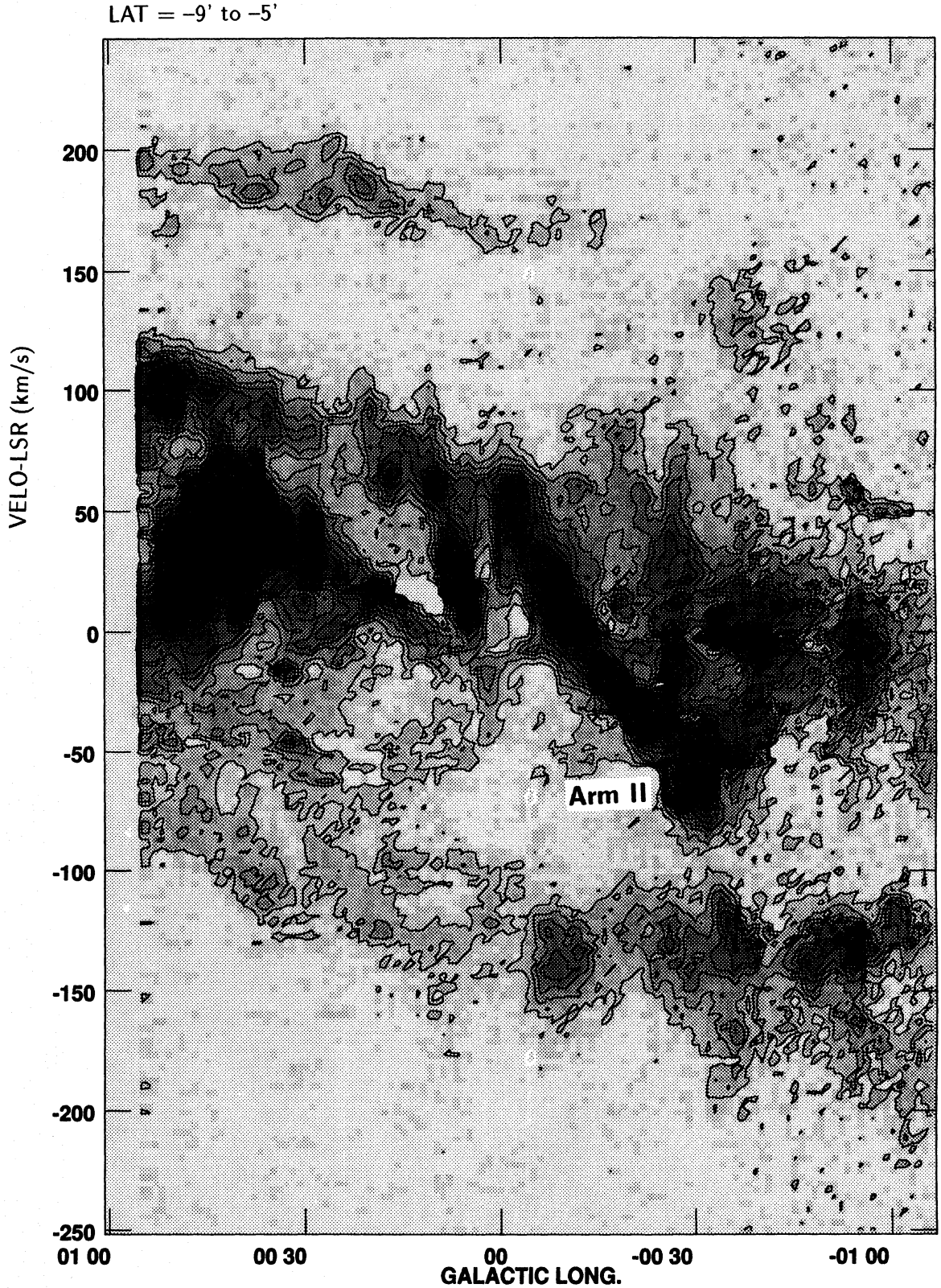

Fig. 2. (l, V) diagrams averaged over the $4'$ b interval. Local/foreground emissions have been removed. 'Rigid-rotation' ridges (arms) are dominant in the disk at $|b| \lesssim 10'$ (25 pc). The contours are in units of K $T_{\rm A}^*$ at levels $0.2\times$(1, 2, 3,..., 9, 10, 12, 14, 16, 18, 20, 25, 30).

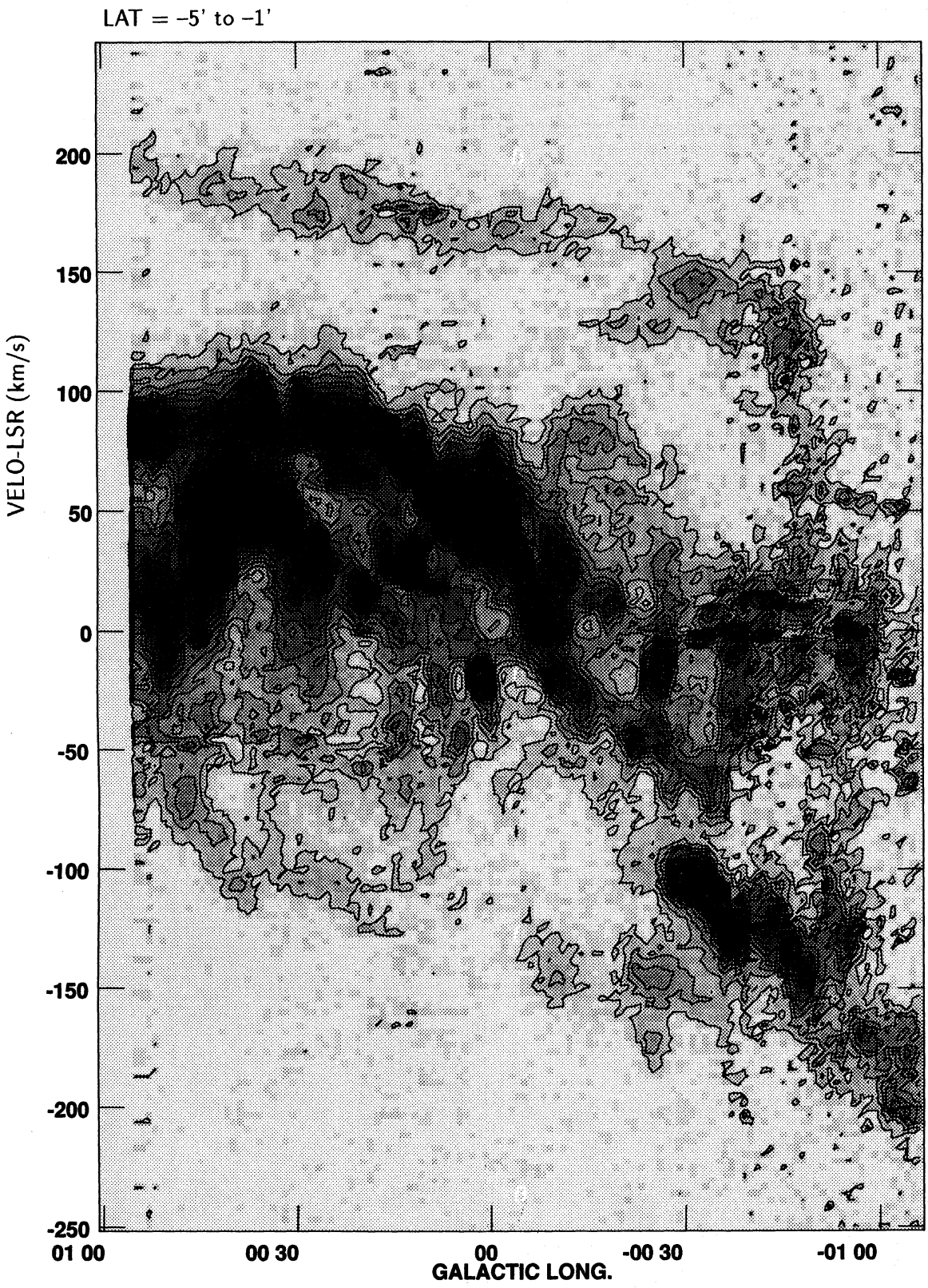

Fig. 2. (continued)

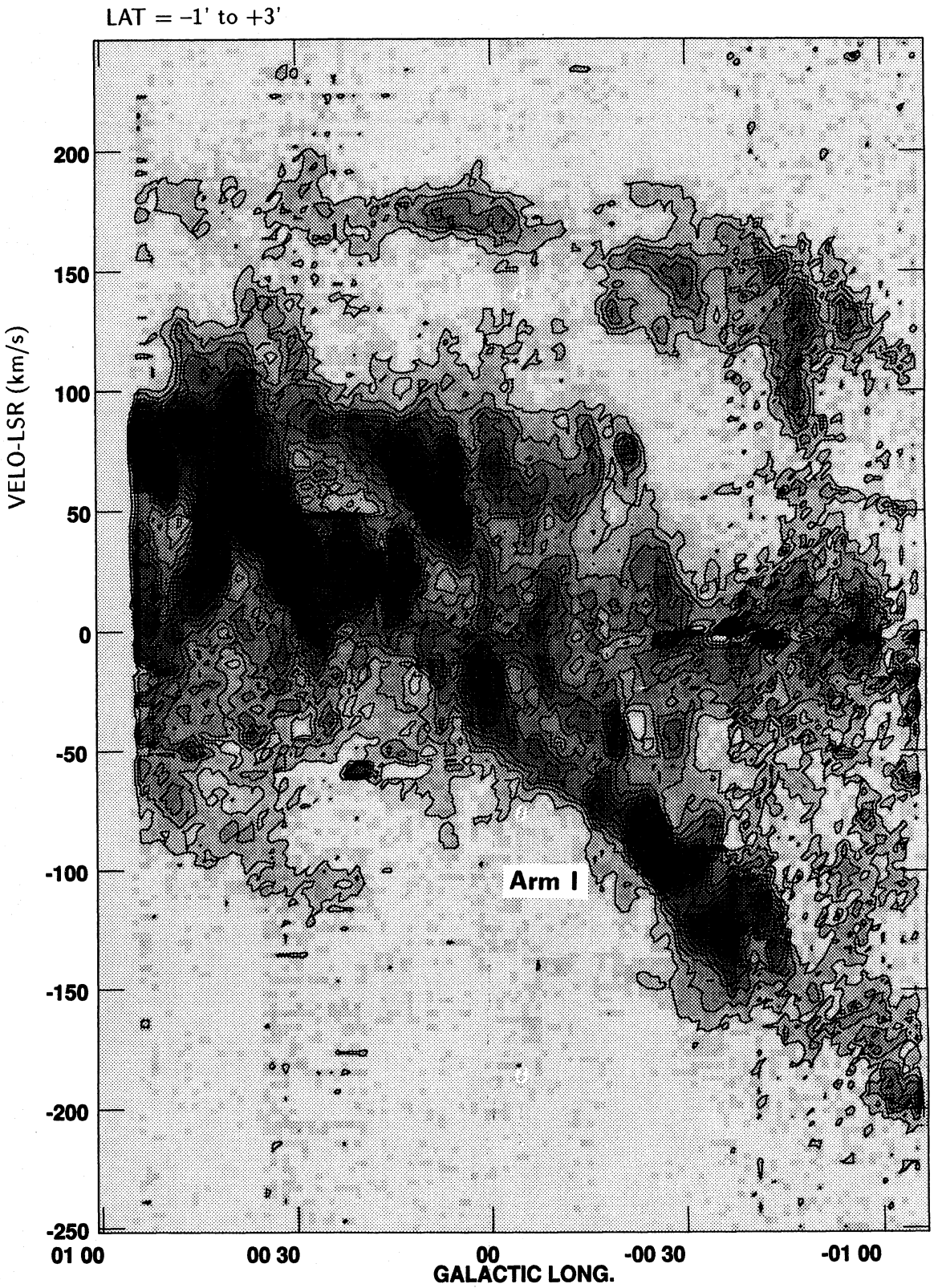

Fig. 2. (continued)

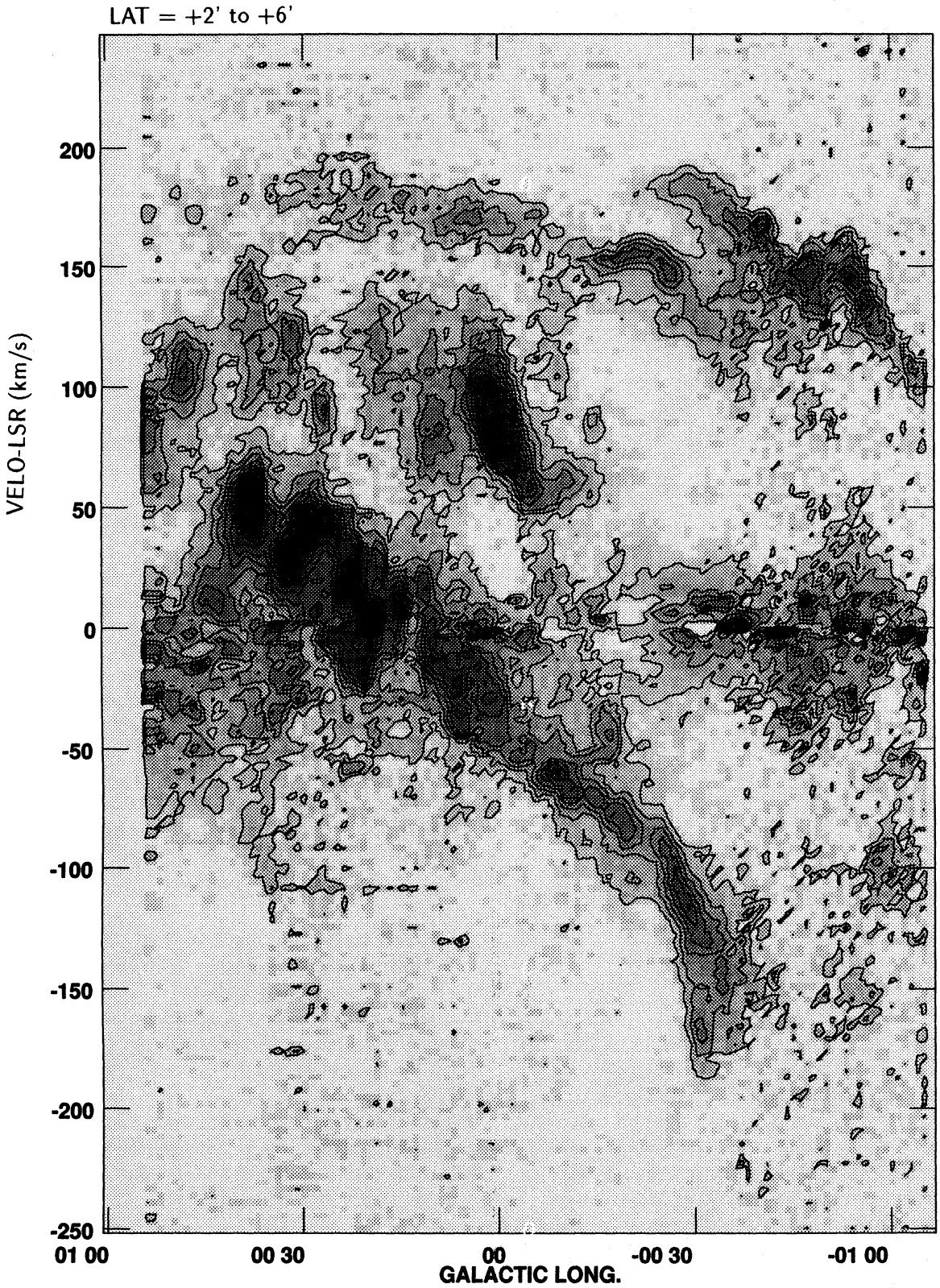

Fig. 2. (continued)

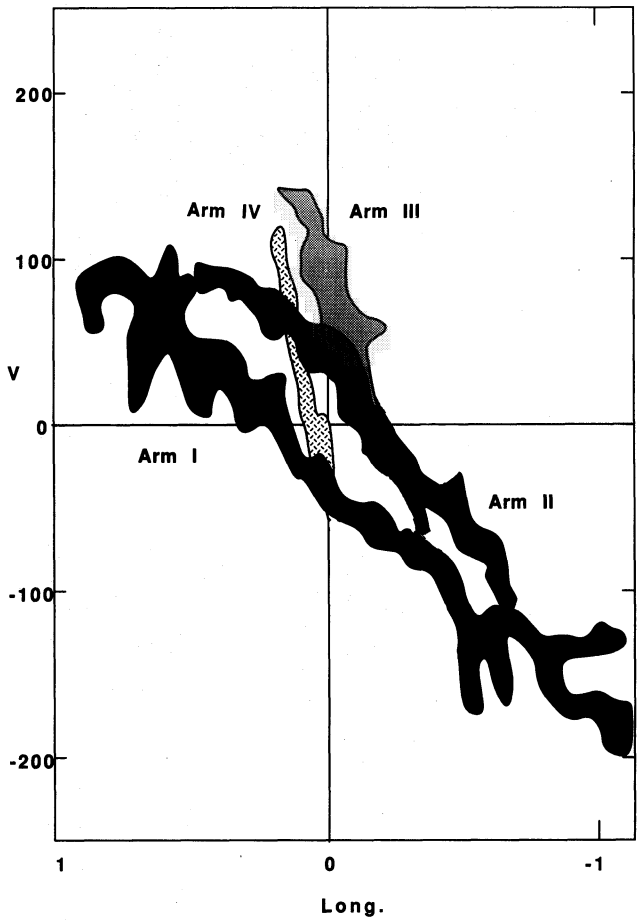

Fig. 3. Schematic sketch of the major ridges (arms) of the (l, V) diagrams.

within individual galaxies, which is almost equivalent to the metallicity dependence. For the Milky Way we have

$$X_{12}(R) = 0.92(\pm 0.2) \times 10^{20} \exp(R/R_e) \times [\mathrm{H_2\ cm^{-2}/K\ km\ s^{-1}}], \quad (1)$$

where $R_e = 7.1$ kpc is the scale radius of the disk. Applying this relation to the Galactic center, we obtain a conversion factor at the Galactic center as $X_{12} = 0.92(\pm 0.2) \times 10^{20}$ [$\mathrm{H_2\ cm^{-2}/K\ km\ s^{-1}}$], about one third of the solar vicinity value. We then assume that the ^{12}CO and ^{13}CO intensities are proportional, and estimate the ratio by averaging the observed intensity ratios for the inner Galaxy at $l \leq 20°$ (Solomon et al. 1979); $I_{^{12}\mathrm{CO}}/I_{^{13}\mathrm{CO}} \simeq 6.2 \pm 1.0$. Then, we obtain a conversion factor for the ^{13}CO line intensity in the galactic center region as $X_{13}(R=0) \simeq 5.7 \times 10^{20}$ [$\mathrm{H_2\ cm^{-2}/K\ kms\ s^{-1}}$], and we use this value throughout this paper.

The correction factor from the H mass to real gas mass is given by $\mu = 1/X = 1.61$, where X is the hydrogen abundance in weight. Here, the following relation has been adopted (Shaver et al. 1983): $Y = 0.28 + (\Delta Y/\Delta Z)Z = 0.34$ in weight, where $Z = 0.02$ is the abundance of the heavy elements and $\Delta Y/\Delta Z = 3$ is the metallicity dependence of the helium abundance Y in the interstellar matter, and so, the hydrogen abundance is $X = 0.62$. So, the surface mass density of molecular gas after correction for the mean weight of gas is given by

$$\sigma \sim 14.6(\pm 3)\ I/\eta\ [M_\odot\ \mathrm{pc^{-2}}], \quad (2)$$

where

$$I \equiv \int T_A^* dv\ [\mathrm{K\ km\ s^{-1}}] \quad (3)$$

is the integrated intensity of the ^{13}CO($J = 1$–0) line emission and $\eta = 0.89$ is the primary beam efficiency of the antenna. The total mass of molecular gas (including He and metals) can be estimated by

$$M\ [M_\odot] = 14.6 \int I/\eta\ dxdy\ [\mathrm{K\ km\ s^{-1}\ pc^2}]. \quad (4)$$

Using these relations, we have estimated the total molecular gas mass in the observed area ($-1°.0 \leq l \leq 0°.92$, $-21' \leq b \leq 17'$), after removing the local and foreground contributions, to be $4.6(\pm 0.8) \times 10^7 M_\odot$. We have also estimated the total molecular mass of the "disk" component, which comprises most of the ridge-like features in the (l, V) diagrams, excluding the expanding ring feature (or the parallelogram) at high velocities ($|V_{\mathrm{LSR}}| \gtrsim 100$–$150$ km s^{-1}). The disk component has the mass $3.9 \times 10^7 M_\odot$, which is 85% of the total in the observed region. On the other hand, the expanding ring (or the parallelogram) shares only $6.7 \times 10^6 M_\odot$ (15%) in the region at $|l| < 1°$ (Sofue 1995b).

3.2. *Ring and Arms in Intensity Maps*

In order to clarify whether each of the arms traced in the (l, V) diagrams (figures 1–3), particularly Arms I and II, is a single physical structure in space, we have obtained a velocity-integrated intensity map in the (l, b) plane for each of the arms. Thereby, we integrated the CO intensity in the velocity ranges, as shown in figure 5, individually for Arms I and II. Figure 6 shows the integrated intensity maps corresponding to Arms I and II, together with a summation of I and II. In table 1 we summarize the derived parameters.

3.2.1. *Galactic-Center Arms I, II*

In the intensity map, Arm I can be traced as a single, thin arc-like arm from $l = 0°.9$ near to Sgr B complex toward negative longitude at $l = -1°.0$. We call this spatial arm the Galactic-Center Arm I (GCA I). The angular

(a)

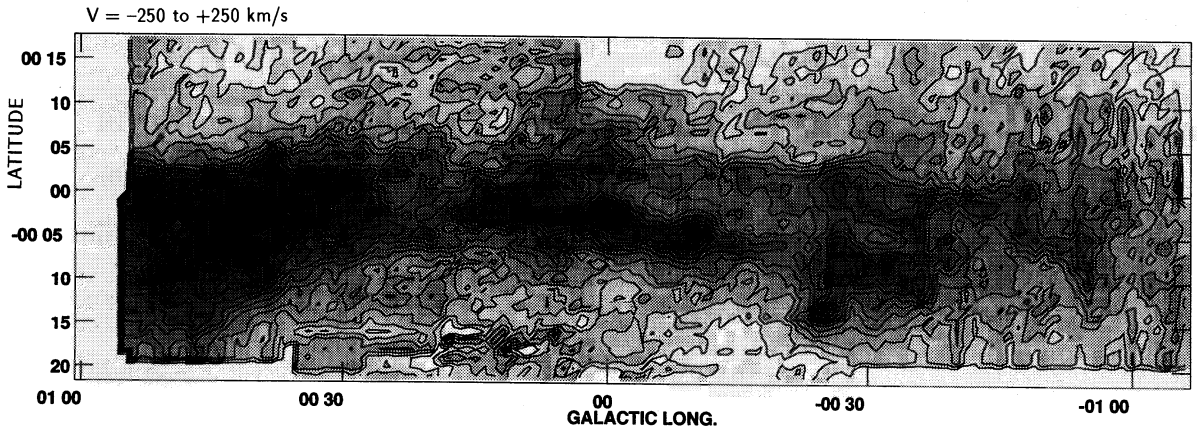

(b)

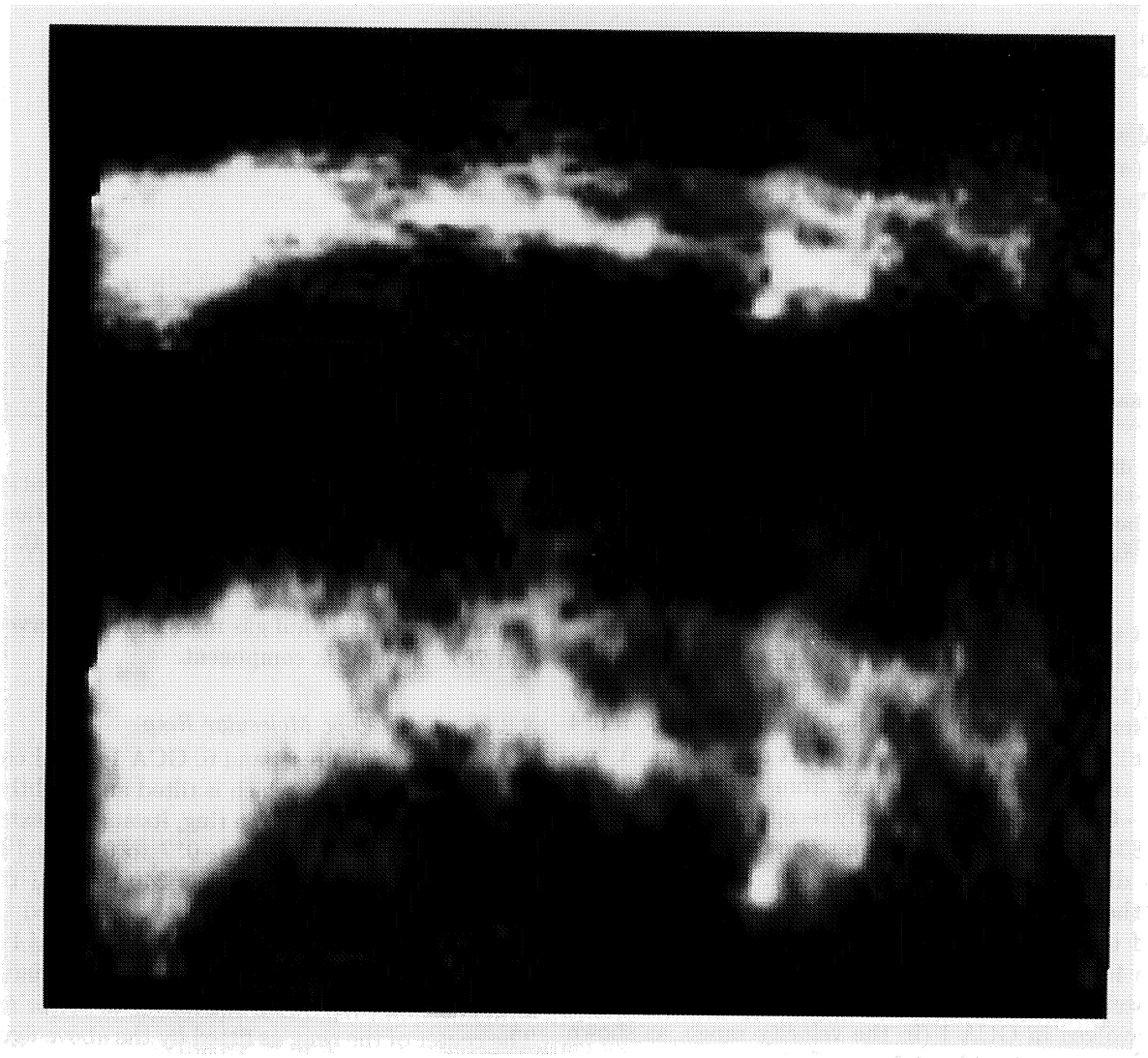

Fig. 4. (a) Integrated-intensity map in the whole velocity range at $-250 \leq V_{\rm LSR} \leq 250$ km s^{-1}. This is almost the same as the map presented by Stark et al. (1989), except that the local contribution has been subtracted. The contours are in units of K km s^{-1} at levels $25\times(1, 2, 3, ..., 9, 10, 12, 14, 16, 18, 20, 25, 30)$. (b) Same, but in a gray-scale representation. For the intensity scale, see (a). The bottom figure shows the same, but the scale in the latitude direction has been doubled. Galactic-Center Arm (GCA) I runs as a long arc in the positive b side; GCA II runs in the negative b side.

Table 1. Galactic-Center Arms and Ring.*

Parameters		Ring (I+II)	Arm I	Arm II	Arm III	Arm IV
From (l, V)	(°, km s^{-1})	(+0.9,90)	(0.9, 80)	(0.1, 60) $\sim$ (1, 100)	(0, 140)	(0.1, 60)
To (l, V)	(°, km s^{-1})	(−0.65, −140)	(−0.7, −150) $\sim$ (−1, −200)	(−0.6, −80)	(−0.15, 10)	(0, −20)
V_{LSR} at $l = 0°$	(km s^{-1})	...	−40	+50	+70	−50
From (l, b)	(°,°).....	(+0.9, 0.0)	(+0.9, −0.1)	(0.25, −0.05)	(0.25, 0.25)	...
To (l, b)	(°,°)	(−0.65, −0.08)	(−1.0, −0.2)	(−0.65, −0.17)	(0, 0)	...
b at $l = 0°$	(°)	...	0.050	−0.067	(0, 0)	...
Length	(°/pc)	...	1.9/280	0.9/133	0.35/52	...
Min. b width	(°/pc).....	...	0.088/13	0.091/13.5	...	...
Max. b width	(°/pc).....	...	0.33/50	0.2/30	...	...
Maj.ax.len.	(°/pc).....	1.55/230	...	...	...	...
Min.ax.len.	(°/pc).....	0.132/19.5	...	...	...	...
Inclination	(°).....	85°.1	...	...	...	...
Ring cen. (l, b)	(°,°)	(0.12,0.0)	...	...	...	...
Ring radius	(pc)	120				
Rot. Velo	(km s^{-1}).....	+90/ − 140	...	...	...	...
Mol. Mass†	($10^7 M_\odot$).....	3.07	1.72	1.35	...	...
Remarks	.....	Circum Nuc.	asso. Sgr B	Sgr C	Sgr A?	Sgr A?

* The distance to the galactic center is assumed to be 8.5 kpc.

† 1.61-times the H_2 mass obtained from the ^{13}CO intensity to H_2 conversion [see equations (1)–(3)], where the metal abundance has been assumed to be twice the solar abundance. The statistical error which occurs during intensity integration is only a few %, while the error arising from ambiguity of the conversion factor is about 20 to 30% (Arimoto et al. 1994).

extent is as long as 1.°9 (280 pc) in the longitudinal direction, whereas the thickness in the b direction is as thin as $\sim 5'$ (13 pc; see subsection 3.2.2). The Sgr B molecular complex is much extended in the b direction by about 0.°4 (60 pc), and comprises a massive part of the arm. A "return" of this arm can be traced from (l, b)=(0.°9, 0°) to (0.°2, −0.°07), and is more clearly recognized in figure 4 at $V = 83$–167km s^{-1}. This can also be clearly seen in the (l, V) diagram in figure 2 at $b \sim -0.°1$. In the negative l side, the arm appears to be bifurcated at $l \sim -0.°65$, and linked to Arm II. This can be more clearly observed in figure 4 at $V = -83$–0 km s^{-1}. The intensity in figure 6a has been integrated to give the total mass of molecular gas involved in GCA I (in the velocity range, as shown in figure 5a) to be $M = 1.72 \times 10^7 M_\odot$.

Arm II can be traced as a a single bright ridge from $l \sim 0.°3$ to $-0.°7$, and the thickness is about $6'$ (15 pc), and makes GCA II. The mass of Arm II is estimated to be $1.35 \times 10^7 M_\odot$. Thus, the total mass involved in GCA I and II is estimated to be $3.07 \times 10^7 M_\odot$, and shares almost 67% of the total gas mass in the observed region, and 78% of the disk component.

3.2.2. *The 120-pc Molecular Ring*

As shown in figures 4 and 6, GCA I and II comprise a global ring structure, which is tilted and slightly bent. If we fit the GCA I and II by a ring, its angular extent in the major axis is 1.°6 from $l = -0.°7$ to 0.°9, and thus, the major-axis length (diameter) is 240 pc, and the radius 120 pc. The minor axis length is estimated to be $7'.9$ from the maximum separation between Arms I and II at $l \sim -0.°2$ (see figure 7). Therefore, the inclination of the I+II ring is $i = 85°$ from the minor-to-major axis ratio. The center of the ring, as fitted by the above figures, is at (l, b)=(0.°1, 0.°0) We call this ring the 120-pc Molecular Ring.

From this information we conclude that the spatial distribution of the molecular gas associated with the principal ridges in the (l, V) diagrams comprises a circum-

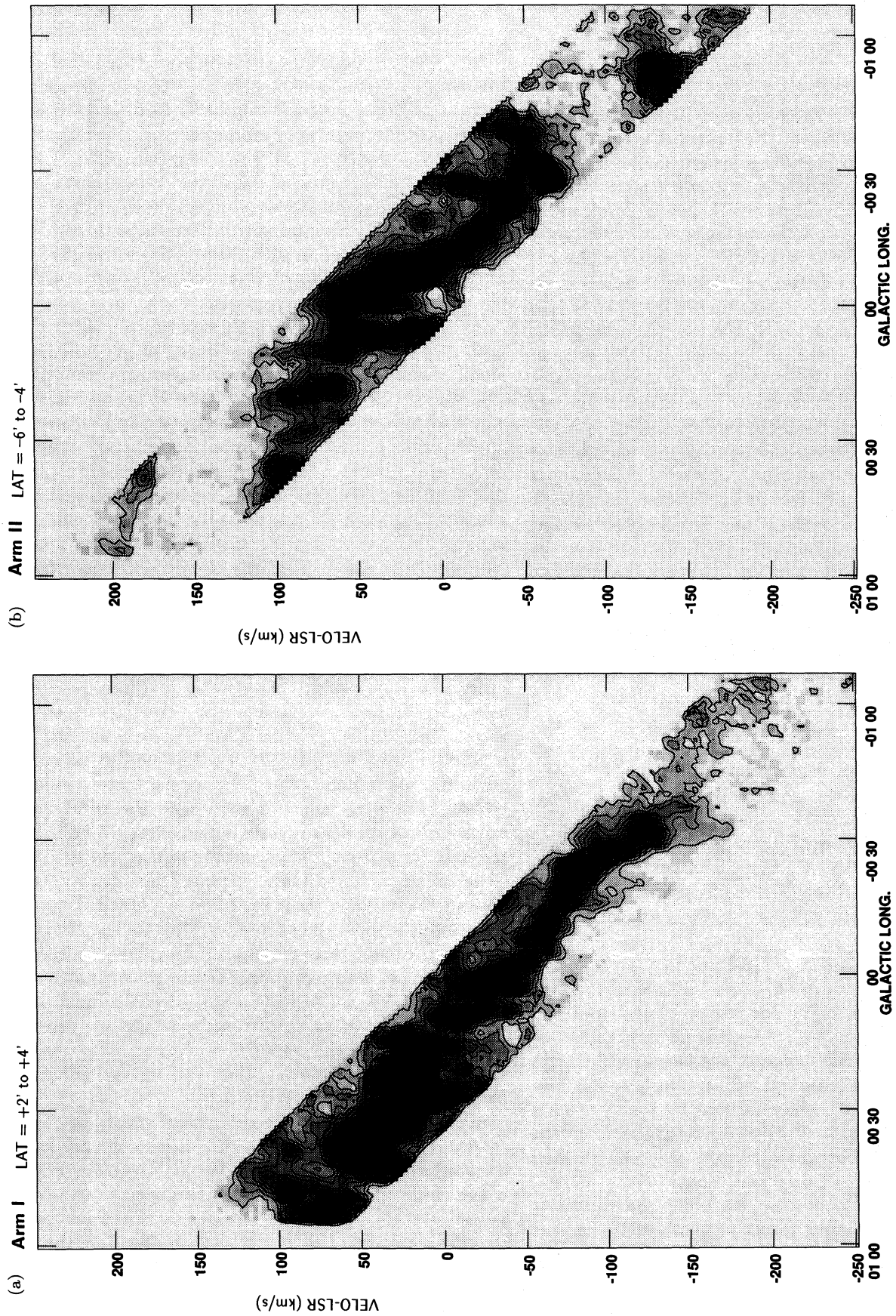

Fig. 5. (l, V) diagrams corresponding to (a) Galactic Center Arms I and (b) II, which were used to obtain intensity maps of the Galactic Center Arms in figure 6. The contours are in units of K T_A^* at levels $0.2\times(1, 2, 3, 4, 5, 6, 8, 10, 12, 15, 20, 25, 30, 35)$.

nuclear ring of radius $R \simeq 120$ pc inclined by 5° from the line of sight.

3.2.3. *Cross section of the Arms*

Figure 7 shows the intensity variation perpendicular to the galactic plane across GCA I and II averaged from $l = 0.°24$ to $-0.°33$, where the arms are most clearly separated. Since the effective resolution of the present data is $(\theta^2 + \Delta b^2)^{1/2} = 2.'0$, where $\theta = 1.'7$ is the beam width and $\Delta b = 1.'0$ is the grid interval, the arms are sufficiently resolved. The two peaks in the figure at $b = 1.'8$ (Arm I) and $b = -6.'0$ (Arm II) can be fitted by a Gaussian intensity distributions as $(T_{\rm B,peak}, {\rm FWHM}) = (0.27\ {\rm K}, 5.'3)$ and $(0.33\ {\rm K}, 5.'5)$, respectively. Namely, the arms are as thin as 13.0 (GCA I) and 13.5 pc (GCA II). If we subtract the contributions from these two arm components, the residual intensity in the whole area in figure 7 is only 36% of the total intensity. The intensity coming from the inter-arm region between the arms shares only 12% of the intensity from the two arms. This would be an upper limit, as the region displayed in this figure is the weakest part along the arms without any significant molecular clumps and condensations. We thus conclude that the molecular gas as observed in the CO line emission in the region discussed in this paper is almost totally confined within the two major arms. Therefore, the central 100 pc radius region is almost empty, making a hole of molecular gas, except for the nuclear few pc region surrounding Sgr A.

3.3. *Velocity Field*

Figure 8a shows the velocity field as obtained by taking the first moment of the $(V_{\rm LSR}, l, b)$ cube, and therefore, an intensity-weighted velocity field. The general rotation characteristics can be clearly seen along the major axis of the ring feature at $b \simeq -6'$. Sgr C molecular spur is seen as a negative-velocity spur extending toward negative b. GCA III is seen as tilted high-velocity plume at $(l, b) \sim (0.°2, 0.°1)$.

In addition to these individual velocity structures, a large-scale velocity gradient in the latitude direction is prominent in the sense that the positive-b side has a positive velocity and the negative-b side has a negative velocity. This can be attributed to the fact that the high-velocity expanding shell (ring) is more clearly seen in positive velocity at $b > 0°$, while the negative velocity part is more clearly seen at $b < 0°$. This can be explained by the tilted nature of the expanding oblate molecular shell on an analysis of the (b, V) diagrams (Sofue 1995b). In fact, if we construct a velocity field, excluding the expanding ring features, we obtain a rather regular velocity field, as shown in figure 8b.

3.4. *Possible Models for the Galactic Center Arms and Ring*

We try to reproduce the (l, V) diagram based on a simple spiral-arm model. According to the galactic shock-wave theory (Fujimoto 1966; Roberts 1969) and the bar-induced shock-wave theory (Sørensen et al. 1976; Huntley et al. 1978; Roberts et al. 1979; Noguchi 1988; Wada, Habe 1992), flow vectors of gas in the densest part along the shocked arms are almost parallel to the potential valley that is rigidly rotating at a pattern speed slower than the galactic rotation. In such shocked flows, the gas cannot be on a closed orbit, but is accreted rapidly toward the center along deformed spirals.

As the simplest approach to simulate an (l, V) diagram, we assume that the flow vector of gas is aligned along a spiral with a constant velocity equal to the rotation velocity in the potential. Figure 9a shows a model where we have assumed two symmetrical spiral arms with a pitch angle $p = 10°$. In addition to a constant circular rotation of gas ($V_{\rm rot}$ =constant; flat rotation curve), radial infall motion of $V_{\rm rot} \sin p$ is superposed, so that the gas is flowing along the arms into the central region. The density distribution in the arms is shown by the spiral-like contours. The azimuthally averaged density of gas has a hole at the center, or corresponds to a ring distribution of gas on which two arms are superposed. A calculated (l, V) diagram is shown by the superposed contours with a tilted X shape. The characteristic features in the observed (l, V) diagrams can now be qualitatively reproduced. Figures 9b and 9c show cases in which the spiral arms are oval in shape, whose major axis is inclined by $\pm 30°$ from the nodal line. Such a case may be expected when the oval potential, or a bar in the center, is deep enough to produce non-circular motion. Figure 9d–f are the same, but the density distribution along the arms has the maximum at the center and the pitch angle is taken to be larger: $p = 20°$. Again, the case of circular rotation appears to reproduce the observation, while the oval orbit cases result in more complicated (l, V) plots than the observation. Among these models, the case shown in figures 9a or 9b appears to reproduce the observed characteristics in the (l, V) plot (e.g. figure 3) reasonably well. The model in figures 9d or 9e with the averaged gas density increasing toward the center may explain the observed Arms III and IV. However, the cases corresponding to figure 9c and 9f may be excluded.

According to the galactic shock-wave theory in a spiral density wave or a bar potential, the shocked gas loses its azimuthal velocity so that the (l, V) behavior becomes closer to the potential's pattern speed. As a consequence, the apparent rotation velocity of the gas along the shocked spiral arms is smaller than that from the rotation velocity. This may be the reason why the observed maximum velocities of the rings/arms (e.g., Arm I near Sgr B) are less than that expected from the gravitational

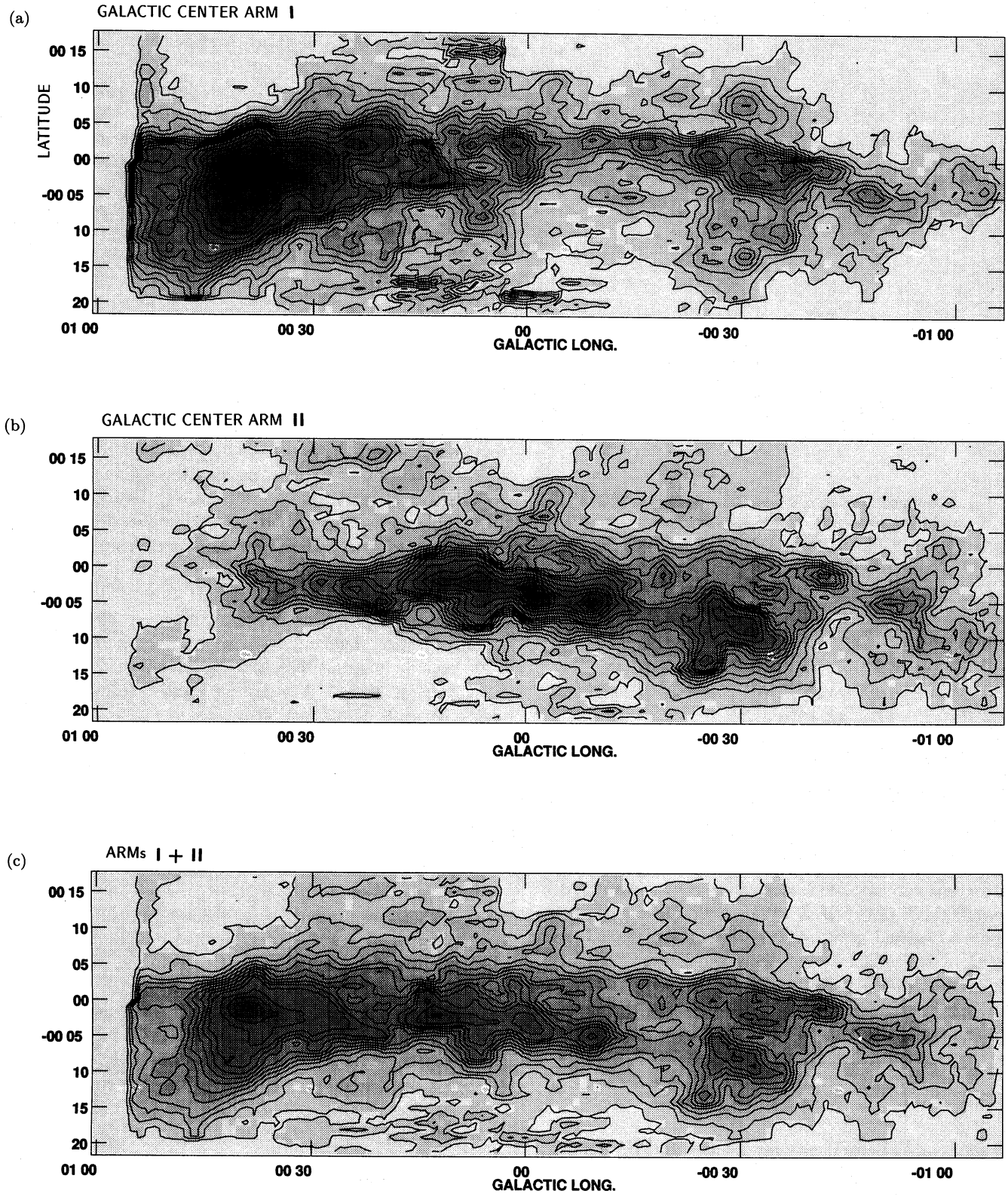

Fig. 6. Integrated intensity maps corresponding to (a) Galactic Center Arm I, and (b) Arm II as in figure 5. The contours are in units of K km s^{-1} at levels 12.5×(1, 2, 3, ..., 9, 10, 12, 14, 16, 18, 20, 25, 30). (c) Arms I+II. The contours are in units of K km s^{-1} at levels 25×(as above).

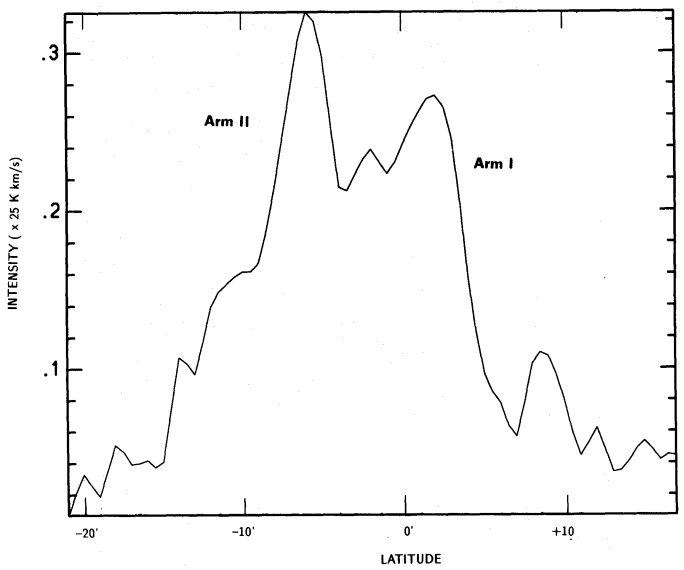

Fig. 7. Intensity variation across Galactic Center Arms I and II perpendicular to the galactic plane averaged at $l = 0.^\circ24$ to $-0.^\circ33$, where the arms are most clearly separated.

potential.

3.5. *Deconvolution into Projection on the Galactic Plane: a Face-on View*

We may thus assume that the molecular gas is on a ring or spiral arms whose pitch angle is not very large. It is then possible to deconvolve the (l, V) diagram into a spatial distribution in the galactic plane by assuming approximately circular rotation. Thereby, we make use of the velocity-to-space transformation (VST), which has been extensively applied to derive the H I gas distribution in our Galaxy (Oort et al. 1958). Suppose that a gas element is located at a projected distance of x ($\simeq l \times 8.5$ kpc) along the galactic plane from the center of rotation, and has a radial velocity v. If the rotation is circular at velocity V_0, the line-of-sight distance y of the element from the nodal line can be calculated by

$$y = \pm|x|\sqrt{\left(\frac{V_0}{v}\right)^2 - 1}. \quad (5)$$

The signs must be opposite for Arms I and II. Here, we assume that Arm I is at the near side, and Arm II at the far side, so that the signs are $-/+$, respectively. The center of rotation is assumed to be at Sgr A, and v is measured from the intersection velocity at $l = -0.^\circ06$ on each arm ridge.

Figure 10 shows a thus-obtained "face-on" map of the molecular gas for $V_0 = 150$ km s^{-1}. The arms appear to construct a circum-nuclear ring of radius ~ 120 pc. Here, we used (l, V) diagrams averaged within latitude ranges $-2' \leq b \leq 6'$ for Arm I and $-5' \leq b \leq 3'$ for Arm II, so that vertically extended clumps, such as the Sgr B complex, are only partly mapped in this figure. During the deconvolution, we used only the arm component concentrated near to the ridges within ± 20 km s^{-1} in velocity (as illustrated in figure 5). Diffuse gas and clumps with velocities far from the arms are not taken into account. The same VST was applied to the H II regions Sgr B1, B2, and C using their H recombination line velocities (Downes et al. 1980). Their positions are plotted in figure 10. The H II regions lie along the arms associated with the molecular complexes, though slightly avoiding the molecular gas peaks. Sgr B and C appear to be at symmetrically opposite locations with respect to the nucleus. We have assumed that Arm I is at the near side. However, in this kind of simple deconvolution, we cannot distinguish the exact orientation, as is the case of the deconvolution of the gas distribution inside the solar circle based on kinematical information. Hence, it may be possible to assume an opposite configuration of the arm locations: Arm I at the far side, and Arm II at the near side.

The connection of Arms I and II is not clear from this deconvolution. This is mainly because of the ambiguous position determination near to the node, which arises from an unknown precise rotation curve. The error is also large at $|l| \lesssim 0.^\circ1$, where we applied interpolation from both sides along each arm. Obviously, this kind of deconvolution is not unique, but was possible here because of the separation of Arms I and II in the (l, b) plane. Therefore, this deconvolution should be taken as a possible hint concerning the spatial distribution of gas.

3.6. *Comparison with Other Galaxies and Models*

Accretion spirals, either shocked or not, and rings of molecular gas have indeed been observed in the CO line in many extragalactic systems, such as IC 342 (Lo et al. 1984; Ishizuki et al. 1990a) and NGC 6946 (Ishizuki et al. 1990b). The ring structure of molecular gas of 100 to a few hundred pc size is commonly observed in the central regions of spiral galaxies (Nakai et al. 1987; Ishiguro et al. 1989). See Sofue (1991) for a greater number of galaxies with a nuclear molecular ring. Thus, the ring/spiral structure of molecular gas of radius 120 pc in the Milky Way, would be similar to the situation found in external galaxies.

There have been various numerical simulations of the accretion of gas toward the central region in spiral and oval potential by gas-dynamical simulations (Sørensen et al. 1976; Huntley et al. 1978; Roberts et al. 1979; Noguchi 1988; Wada, Habe 1992). The models predict a rapid accretion of gas along the spiral orbits; the gas behavior

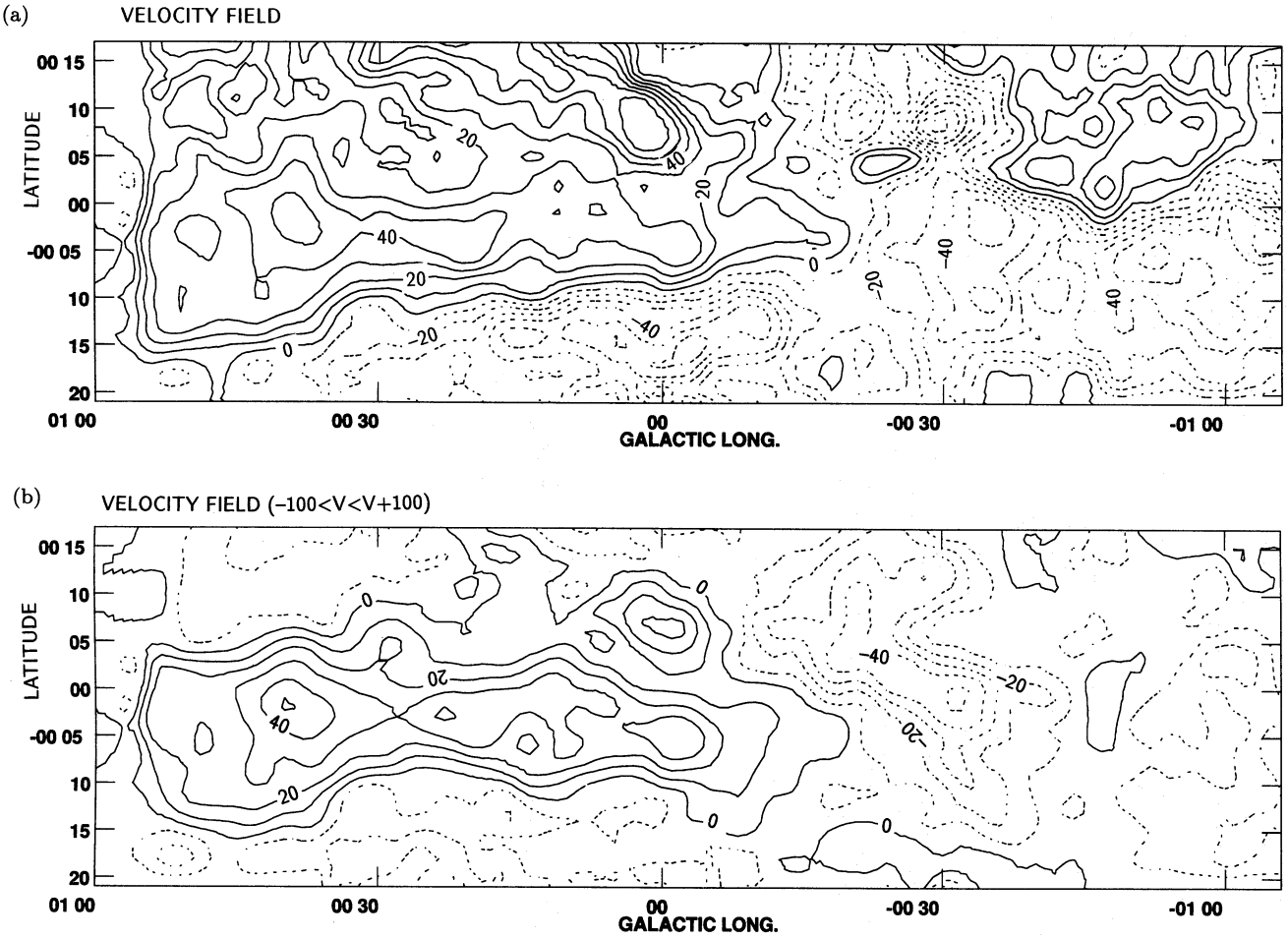

Fig. 8. (a) Velocity field as obtained by taking the first moment of the $(V_{\rm LSR}, l, b)$ cube (intensity-weighted mean velocity field). The contour interval is 10 km s^{-1}. The full-line contours are for positive velocity starting at 0 km s^{-1}. The dashed contours are for negative velocity. (b) Same as (a), but for the "disk component" with $|V_{\rm LSR}| < 100$ km s^{-1}.

in these models somehow mimics the models illustrated in figure 9.

A number of simulations of position-velocity diagrams along the galactic plane have been constructed and compared with the observations, in order to understand the larger-scale (l, V) diagrams for our Galaxy both in H I and CO (Mulder, Liem 1986; Liszt, Burton 1978; Burton 1988). Position-velocity diagrams for extragalactic edge-on galaxies in CO have been extensively studied (Sofue, Nakai 1993, 1994; Sofue 1995a) and a numerical simulation has been attempted to reproduce the PV characteristics based on the gas dynamics in an oval potential (e.g., Mulder, Liem 1986; Wada et al. 1995).

Binney et al. (1991) have noticed a "parallelogram" and calculated theoretical (l, V) diagrams; they have shown the presence of a bar of 2 kpc length in the Galactic bulge. However, the parallelogram (the expanding ring feature) in figure 1b shares only 15% of the total emission. However, we emphasize that the major structures, which contain 85% of the molecular mass within 150 pc of the center, are due to the Arms discussed above.

3.7. Relationship with Radio Sources

Figure 11 shows a superposition of a 10-GHz radio continuum map (Handa et al. 1987) on the ^{13}CO and CS intensity maps. Here, we briefly comment on the global relationship of the major radio sources with molecular features at a spatial resolution of a few arc minutes. The detailed internal structures of individual sources are out of the scope of the present paper, for which the readers may refer to a review by Liszt (1988).

3.7.1. Sgr A

The relationship between the molecular features at scales less than a few arc minutes with Sgr A has been discussed by many authors (e.g., Oort 1977; Bally et al. 1987; Güsten 1989). However, these nuclear features,

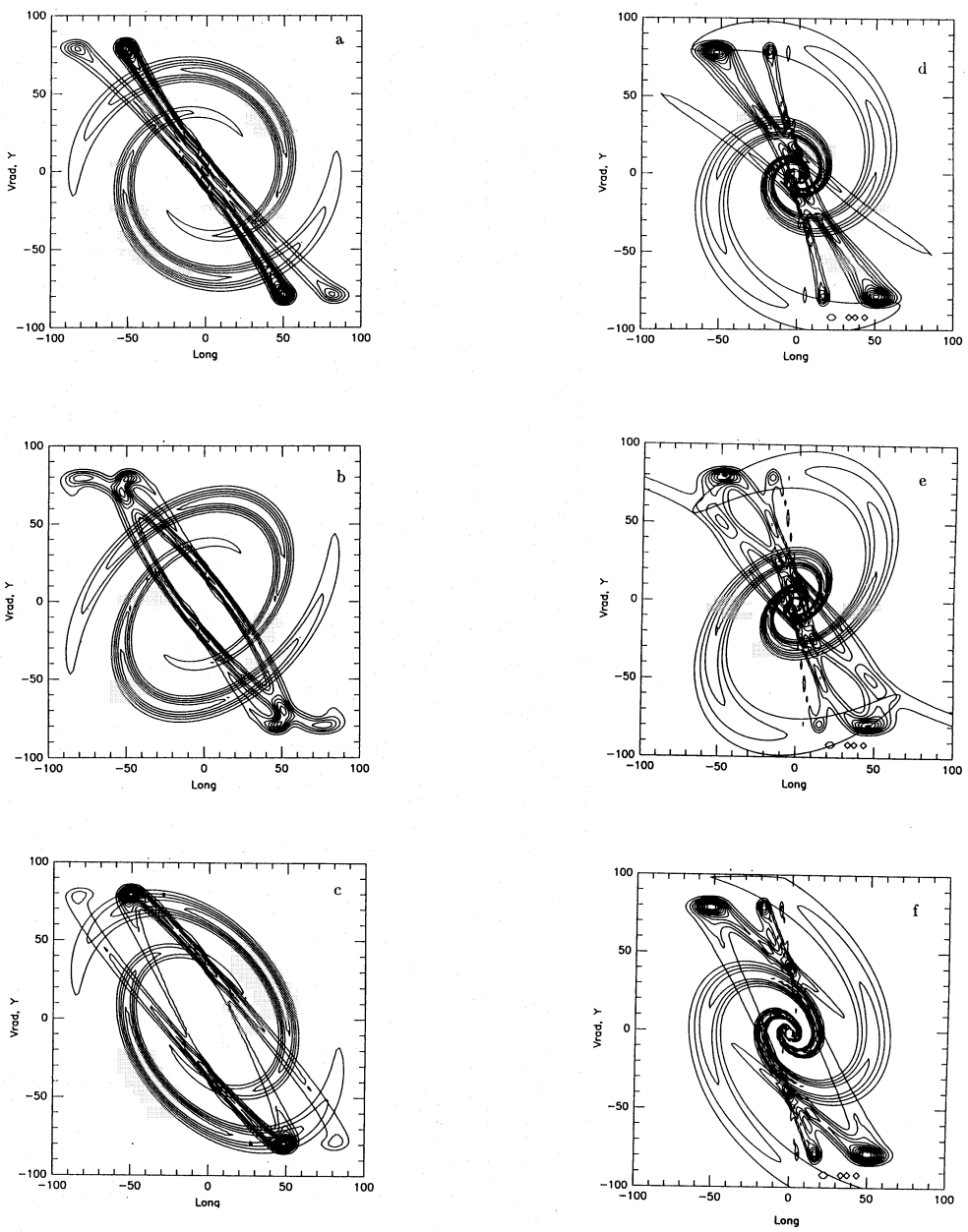

Fig. 9. Two-armed spiral model with a spiral infalling motion. The gas density distribution is shown by the spiral-like contours as projected on the galactic plane. The calculated (l, V) diagram is shown by tilted X shaped contours. The scales are arbitrary. (a) Two spiral arms with a pitch angle p of 10° are assumed. The azimuthally averaged gas density has a hole at the center, corresponding to a ring distribution of gas on which two arms are superposed. In addition to a constant circular rotation, radial infall of velocity $V_{\rm rot}$ sin p is superposed. (b), (c) The same as (a), but the spiral arms are oval in shape whose major axis are inclined by ±30° from the nodal line. (d)–(f) The same as (a)–(c), respectively, but the density distribution along the arms has the maximum at the center and the pitch angle is taken larger: $p = 20°$.

which are of 1′ (∼ 3 pc) scales, are not well visible in the present plots, so far as the (l, V) plots are concerned. We only mention that Arm III is a largely tilted out-of-plane plume with a high positive velocity, which Bally et al. (1988) called the polar arc. Arm IV also shows a large velocity gradient, and appears to be an object related to a deep gravitational potential around the nucleus.

3.7.2. Sgr B

The molecular complex at $l \sim 0.^\circ6$–$0.^\circ9$ on Arm I is associated with the star-forming regions Sgr B1 at $(l, b) = (0.^\circ519, -0.^\circ050)$ and Sgr B2 at $(0.^\circ670, -0.^\circ036)$.

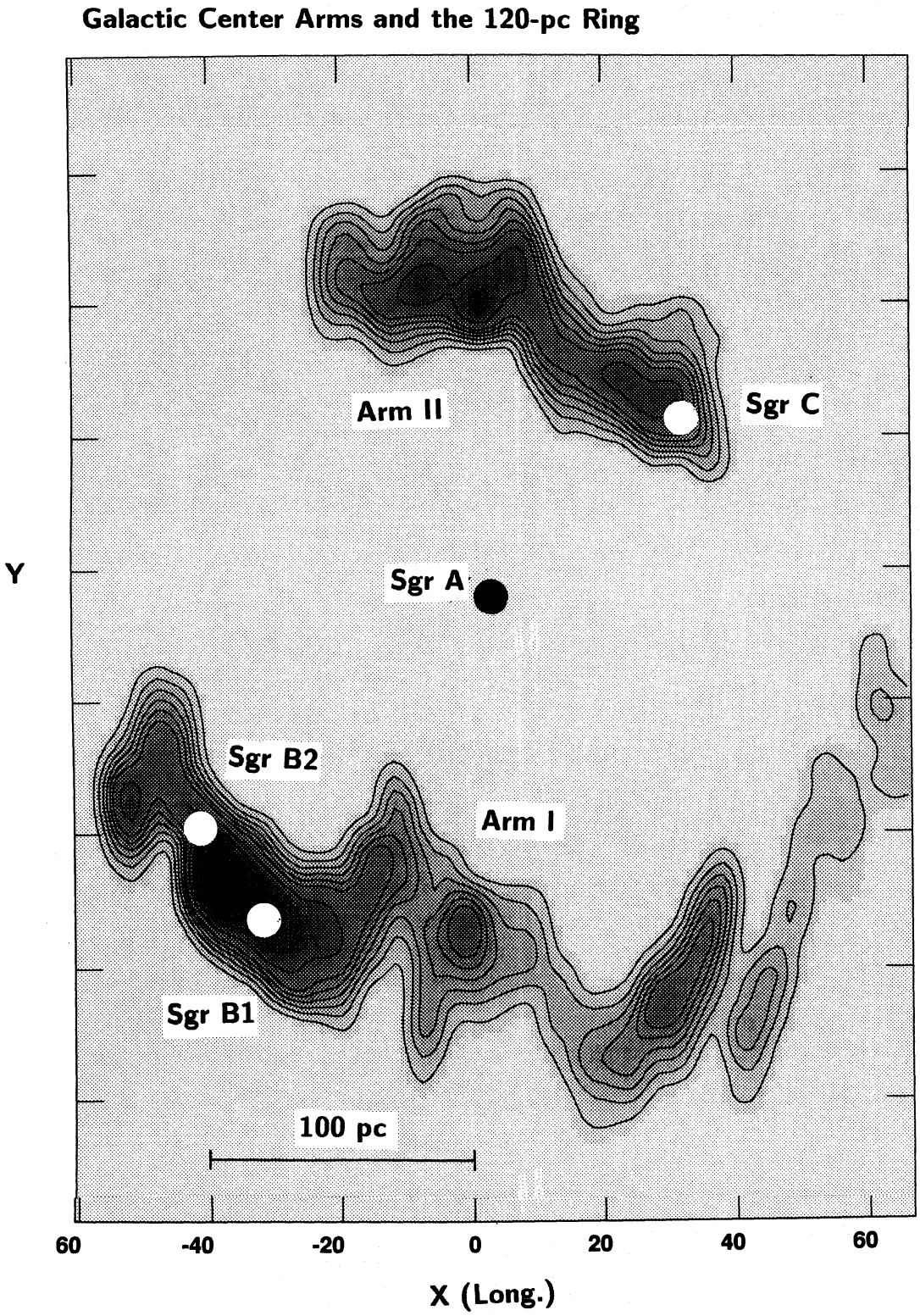

Fig. 10. Possible deconvolution of the (l, V) diagrams for Galactic Center Arms I and II into a spatial distribution as projected on the galactic plane. The contour interval is 0.25 starting at 0.1 in an arbitrary unit. A is assumed to be at the center.

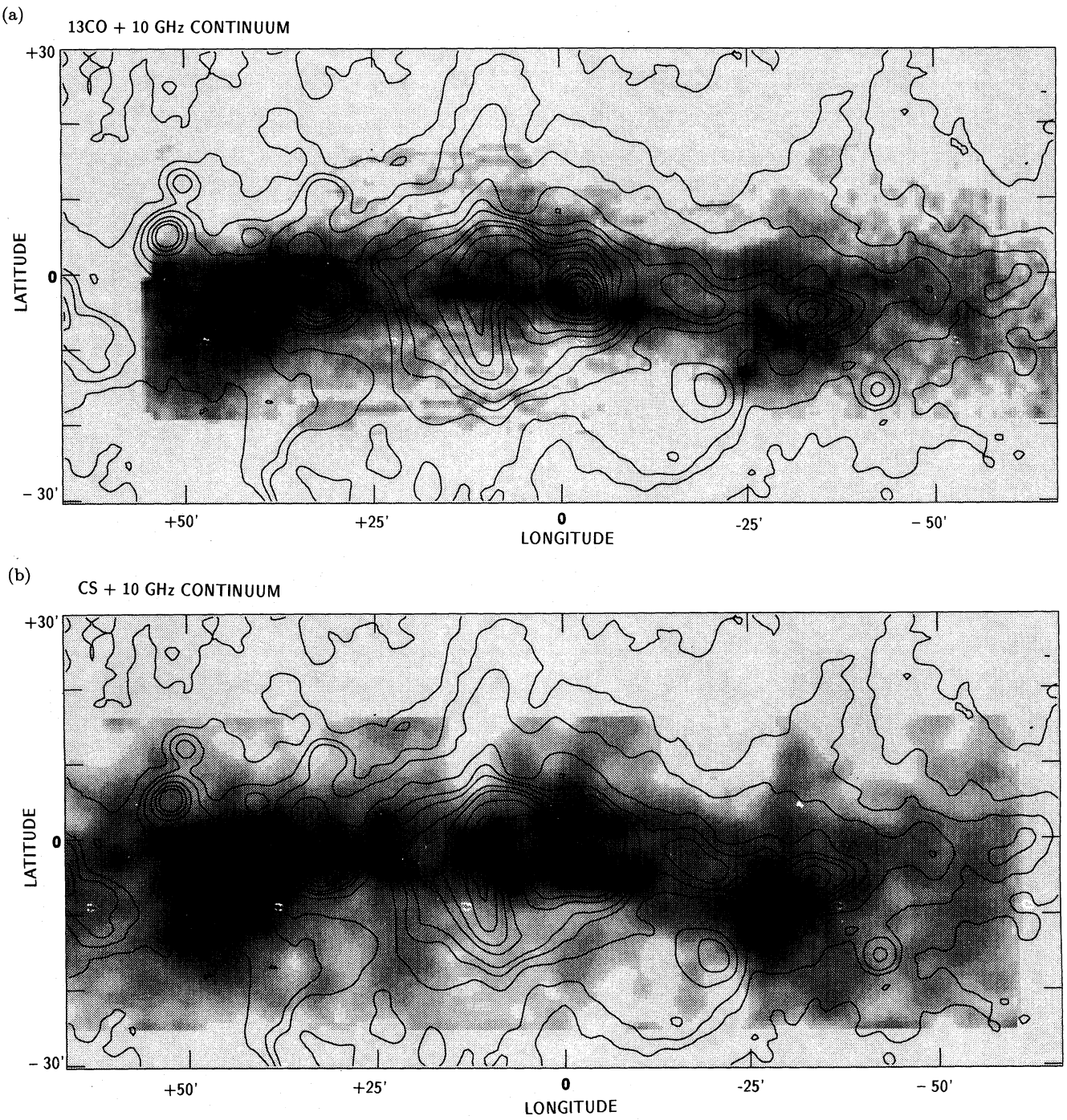

Fig. 11. Superposition of the radio continuum emission at 10 GHz (contours: Handa et al. 1987) on (a) ^{13}CO, and (b) CS emission maps (gray scale). The contours are in units of K T_B of 10 GHz continuum brightness at levels 0.1×(1, 2, 3, 4, 6, 8, 10, 15, 20, 25). For CO intensity scale, see figure 4.

Sgr B1 and B2, whose radial velocities in H recombination line emission are V_{LSR}=45 and 65 km s^{-1}, respectively (Downes et al. 1980), are also located in the (l, V) plane at the upper (higher-velocity) edges of molecular clumps. Thus, the de-convolved positions of these continuum sources are slightly displaced from the de-convolved arm, as indicated in figure 10. The molecular-gas distribution is highly extended in the direction of latitude for about 0.°4 (60 pc), largely shifted toward the lower side of the galactic plane ($b < 0°$). This complex is also

greatly extended in velocity space: the velocity dispersion amounts to as high as 50 km s^{-1}. The internal structure of the Sgr B molecular complex has been discussed in detail in relation to star-formation activity, and it was shown that the molecular gas is distributed in a shell, spatially surrounding the continuum peak (Bally et al. 1988; Sofue 1990; Hasegawa et al. 1993). The present ring model is consistent with the C II line (l, V) diagram, as obtained by Okuda et al. (1989), which indicates a rotating ionized gas feature with Sgr B and C on the tangential points of the ring.

3.7.3. Sgr C

The star-forming region Sgr C is associated with a molecular complex, and is located on Arm II at $l \sim -0.^\circ6$. However, the spatial proximity is less significant than that for Sgr B. The radio continuum peak of Sgr C, $(l, b, V_{\rm LSR}) = (-0.^\circ57, -0.^\circ09)$, is located at the western edge of the molecular complex, but is displaced by about $6'$ (15 pc) from the molecular peak. The LSR velocity of the H recombination line also agrees with the molecular-gas velocity, and thus, is located on the de-convolved arm in figure 10. The molecular gas in this complex is extended vertically, and molecular spurs are found to extend both toward positive and negative latitude directions. We emphasize that the positive-latitude spur is clearly associated with the inner edge of the western ridge of the Galactic Center Lobe observed in the radio continuum emission (Sofue, Handa 1984; Sofue 1985), as is shown in figure 11.

3.8. Orbital Displacement vs Alignment of Star-forming Regions and Molecular Arms

The close association of Sgr B and C with GCA I and II may have a crucial implication for the orbits of gas and stars. If the arms are shock lanes in a bar during highly non-circular motion, the H II regions which occurred a million years old should already be displaced from the molecular arms. Therefore, the fact that Sgr B and C are still near the gas complexes from which they may have been born (after one or more rotations) can be explained only if the stars and gas are circularly co-rotating in the arms at a small pitch angle. This would argue for the validity of the deconvolution process applied in subsection 3.5.

Consider a spiral arm which is a shocked density wave. Star formation from a molecular cloud will be triggered in the arms. It could take about $t \sim 10^6$ yr for protostars to form and shine as OB stars, and, therefore, until H II regions are produced. On the other hand, the rotation period of the stars is only $\sim 10^6$ yr for $r = 100$ pc and $V_{\rm rot} = 200$ km s^{-1}. According to the density wave theory, the velocity difference between the rotation velocity and the shocked gaseous arm, which is about the same as the pattern speed of density wave, is on the order of

$$V_{\rm rot} - V_{\rm p} = (\Omega_{\rm rot} - \Omega_{\rm p})r. \quad (6)$$

The azimuthal phase difference between the H II region and the gaseous arm is then

$$\Delta\phi \sim (\Omega_{\rm rot} - \Omega_{\rm p})t. \quad (7)$$

The phase difference for Sgr B2 and its corresponding molecular peak in figure 10 (darkest part in Arm I) is roughly $\Delta\phi \sim 5^\circ$; a similar value is found for Sgr C. If $t \sim 10^6$ yr, we obtain $\Omega_{\rm rot} - \Omega_{\rm p} \sim 0.1$ radian/10^6 yr ~ 100 km s^{-1} kpc^{-1}. This is an order of magnitude greater than the value near the solar circle (~ 10 km s^{-1} kpc^{-1}). For older H II regions (weaker radio sources) the phase difference would be much greater. Moreover, orbits of stars, and, therefore, H II regions, are no longer closed, and must be largely displaced from the orbits of gas. Thus, the H II regions in the central 100 pc of the Galaxy, except for young cases as Sgr B2, would not be associated with molecular gas arms. This will simply explain why the molecular gas features are not directly correlated with the weaker radio sources in the Galactic center (figure 11).

4. Discussion

By analyzing the ^{13}CO line BTL data cube, we have shown that most (85%) of the total molecular gas within $|l| < 1^\circ$ comprises rigid-body-like structures in the (l, V) diagrams, which can be attributed to arms on a ring. Moreover, 66% of the total gas in the region, and 78% of the disk component ($|b| \lesssim 10'$=25 pc), was found to be confined in the two major Arms, I and II. The spiral/ring structures are consistent with the picture drawn by Scoville et al. (1974) based on earlier data, while the scale obtained here is slightly smaller. The structures will be common in external galaxy nuclei in the sense that the gas distribution is spiral- and ring-like.

Numerical simulations for a few kpc-scale disks have suggested that the features can be understood as the consequence of spiral accretion by a density wave in an oval potential, either shocked or not. Based on a qualitative consideration, we have suggested possible models to explain the observed (l, V) features, as shown in figure 9a.

The molecular mass in the Galactic Center has been derived by using the most recent CO-to-H_2 conversion factor, about one third of the conventional value, which has been obtained by detailed analyses of the dependency on the metallicity as well as on the galacto-centric distance (Arimoto et al. 1994). This has resulted in a factor-of-three smaller mass and energetics than the so-far quoted values in the literature. The molecular mass within 150 pc radius from the center is estimated to be only $3.9 \times 10^7 M_\odot$.

Thus, the molecular-gas mass is only a few percent of the total mass in the region estimated as $M_{\rm dyn} = RV_{\rm rot}^2/G \sim 8 \times 10^8 M_\odot$ for a radius R of ~ 150 pc and a rotation velocity $V_{\rm rot}$ of ~ 150 km s^{-1}. This implies that the self-gravity of gas is not essential in the galactic center, and a given-potential simulation would be sufficient to theoretically understand the behavior of gas.

The expanding molecular ring (or the parallelogram) was shown to share only 15% of the total gas mass within the central 1° region. This feature has been shown to extend vertically over ~ 100 pc above and below the galactic plane (Sofue 1989; Sofue 1995b). Regarding the very different b distribution, it is a clearly distinguished structure from the arms and the ring described in this paper. On the (l, V) plot, the expanding feature can be fitted by an ellipse of radius 1°.2 (Bally et al. 1987), which is larger than the disk discussed in this paper. There have been controversial interpretations about this feature: either it is due to some explosive event (Scoville et al. 1972; Kaifu et al. 1972, 1974) or due to a non-circular rotation of disk gas (Burton, Liszt 1992; Binney 1991). We will discuss this feature based on the present data in a separate paper.

The author would like to express his sincere thanks to Dr. John Bally for making himself available along with the molecular line data in a machine-readable format.

References

Altenhoff W. J., Downes D., Pauls T., Schraml J. 1978, A&AS 35, 23

Arimoto N., Sofue Y., Tsujimoto T. 1994, ApJ submitted

Bally J., Stark A.A., Wilson R.W., Henkel C. 1987, ApJS 65, 13

Bally J., Stark A.A., Wilson R.W., Henkel C. 1988, ApJ 324, 223

Binney J.J., Gerhard O.E., Stark A.A., Bally J., Uchida K.I. 1991, MNRAS 252, 210

Brown R.L, Liszt H.S. 1984, ARA&A 22, 223

Burton W.B. 1988, in Galactic and Extragalactic Radio Astronomy, 2nd ed G.L. Verschuur, K.I. Kellermann (Springer-Verlag, New York) p295

Burton W.B., Liszt H.S. 1983, in Surveys of the Southern Galaxy, ed W.B. Burton, F.P. Israel (Reidel Pub. Co., Dordrecht) p149

Burton W.B., Liszt H.S. 1992, A&AS 95, 9

Combes F. 1992, ARA&A, 29, 195

Cox P., Laureijs R. 1989, in The Center of the Galaxy, IAU Symp 136, ed M. Morris (D. Reidel Publ. Co., Dordrecht) p121

Dame T.M., Ungerechts H., Cohen R.S., de Geus E.J., Grenier I.A., May J., Murphy D.C., Nyman L.-Å. et al. 1987, ApJ 322, 706

Downes D., Wilson T.L., Beiging J., Wink J. 1980, A&AS 40, 379

Fujimoto M. 1966, in Non-stable Phenomena in Galaxies, IAU Symp No 29, ed Arakeljan (Academy of Sciences of Armenia, USSR) p453

Genzel R., Townes C.H. 1987, ARA&A 25, 377

Güsten R. 1989, in The Center of the Galaxy, IAU Symp 136, ed M. Morris (D. Reidel Publ. Co., Dordrecht) p89

Handa T., Sofue Y., Nakai N., Inoue M., Hirabayashi H. 1987, PASJ 39, 709

Hasegawa T., Sato F., Whiteoak J.B., Miyawaki R. 1993, ApJL 419, L77

Heiligman G.M. 1987, ApJ 314, 747

Huntley J.M., Sanders R.H., Roberts W.W. 1978, ApJ 221, 521

Ishiguro M., Kawabe R., Morita K.-I., Okumura S.K., Chikada Y., Kasuga T., Kanzawa T., Iwashita H. et al. 1989, ApJ 344, 763

Ishizuki S., Kawabe R., Ishiguro M., Okumura S.K., Morita K.-I., Chikada Y., Kasuga T. 1990a, Nature 344, 224

Ishizuki S., Kawabe R., Ishiguro M., Okumura S.K., Morita K.-I., Chikada Y., Kasuga T., Doi M. 1990b, ApJ 355, 436

Kaifu N., Iguchi T., Kato T. 1974, PASJ 26, 117

Kaifu N., Kato T., Iguchi T. 1972, Nature 238, 105

Knapp G.R., Stark A.A., Wilson R.W. 1985, AJ 90, 254

Liszt H.S. 1988, in Galactic and Extragalactic Radio Astronomy, ed G.L. Verschuur, K.I. Kellermann, 2nd ed (Springer-Verlag, New York) p359

Liszt H.S., Burton W.B. 1978, ApJ 226, 790

Liszt H.S., Burton W.B. 1980, ApJ 236, 779

Lo K.Y., Berge G.L., Claussen M.J., Heiligman G.M., Leighton R.B., Masson C.R., Moffet A.T., Phillips T.G. et al. 1984, ApJL 282, L59

Mulder W.A., Liem B.T. 1986, A&A 157, 148

Nakai N., Hayashi M., Handa T., Sofue Y., Hasegawa T., Sasaki M. 1987, PASJ 39, 685

Noguchi M. 1988, A&A, 203, 259

Okuda H., Shibai H., Nakagawa T., Matsuhara T., Maihara T., Mizutani K., Kobayashi Y., Hiromoto N. et al. 1989, in The Center of the Galaxy, IAU Symp 136, ed M. Morris (D. Reidel Publ. Co., Dordrecht) p145

Oort J.H. 1977, ARA&A 15, 295

Oort J.H., Kerr F.J., Westerhout G. 1958, MNRAS 118, 379

Roberts W.W. 1969, ApJ 158, 123

Roberts W.W., Huntley J.M., van Albada G.D. 1979, ApJ, 233, 67

Scoville N.Z. 1972, ApJL 175, L127

Scoville N.Z., Solomon P.M., Jefferts K.B. 1974, ApJL 187, L63

Shaver P.A., McGee R.X., Newton L.M., Danks A.C., Pottasch S.R. 1983, MNRAS, 204, 53

Sofue Y. 1985, PASJ 37, 697

Sofue Y. 1989, in The Center of the Galaxy, IAU Symp 136, ed M. Morris (D. Reidel Publ. Co., Dordrecht) p213

Sofue Y. 1990, PASJ 42, 827

Sofue Y. 1991, PASJ 43, 671

Sofue Y. 1995a, ApJ in press

Sofue Y. 1995b, PASJ 47, 551

Sofue Y., Handa T. 1984, Nature 310, 568

Sofue Y., Nakai N. 1993, PASJ 45, 139

Sofue Y., Nakai N. 1994, PASJ 46, 147

Sofue Y., Reich W. 1979, A&AS 38, 251

Solomon P.M., Scoville N.Z., Sanders D.B. 1979, ApJL 232, L89
Sørensen S.-A., Matsuda T., Fujimoto M. 1976, Ap&SS 43, 491
Stark A.A., Bally J., Wilson R.W., Pound M.W. 1989, in The Center of the Galaxy, IAU Symp 136, ed M. Morris (D. Reidel Publ. Co., Dordrecht) p213
Tsuboi M. 1989 in The Galactic Center, IAU Symp 136, ed M. Morris (D. Reidel Publ. Co., Dordrecht) p135
Wada K., Habe A. 1992, MNRAS 258, 82
Wada K., Habe A., Taniguchi Y., Hasegawa T. 1995, ApJL 437, L123